MAE 155A Team 2

Conceptual Design Review

Blended Wing Body – Manta

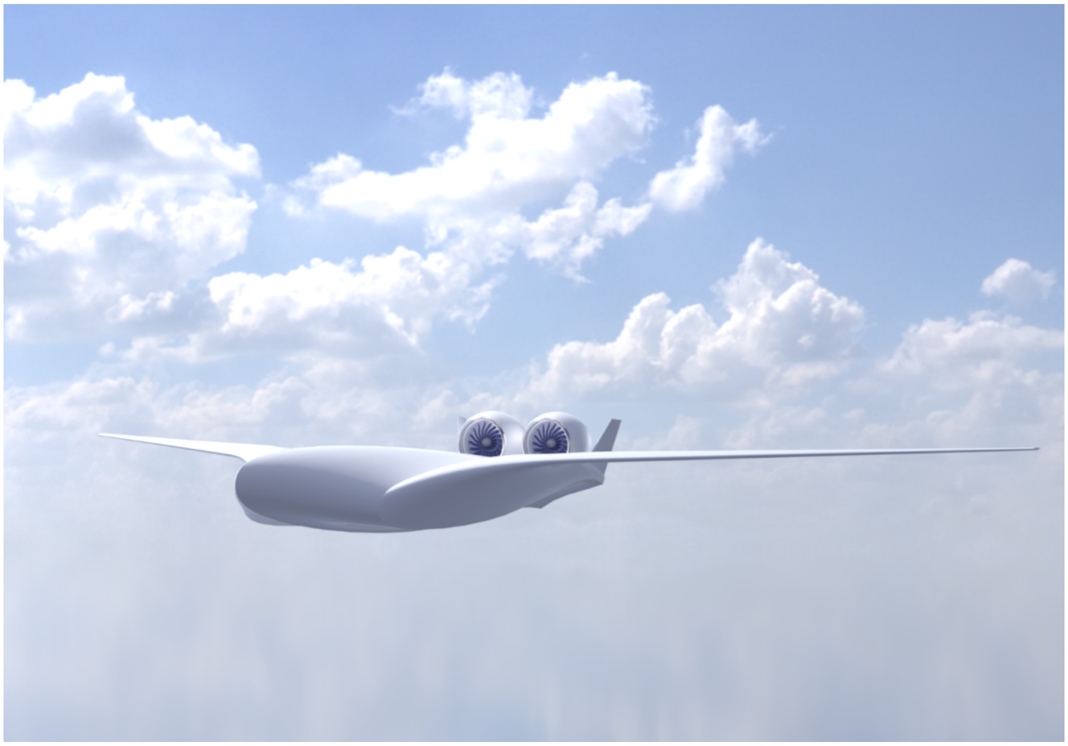

University of California, San Diego

Alexander Burns, Martina Danieli, Anthony Gaeta
Sainirnay Mantrala, Sahil Savasere, Gregorio Zaltzman

March 18, 2026

Contents

1. Executive Summary

1.1 Background and Motivation

Fuel efficiency has improved significantly since the early years of aviation, but has largely plateaued in recent years. With commercial aviation currently accounting for 2.4% of global CO_2 emissions and fuel consumption greatly influencing operating costs, fuel efficiency remains a primary focus of the industry [R1]. Therefore, significant demand is present for a hyper-fuel-efficient aircraft that moves beyond conventional aircraft architecture. This paper proposes a Blended Wing Body (BWB) aircraft to make remarkable strides in fuel efficiency, demonstrating the inherent advantages of a central lifting body over traditional Tube and Wing (TAW) designs. An overview of its specifications is presented in Table 1.

Table 1: Key aircraft specifications of the proposed BWB aircraft prototype.

Range [nmi]	**Cruise Mach**	**Altitude [ft]**	**Capacity [pax]**	**Wingspan [m]**	**AR**	**CASM [$]**	**MTOW [N]**	**Engine Type**	**Cruise L/D**
7400	0.85	40,000	250	64.7	5.03	0.0873	1,435,400	GEnX-1B	25.30

The proposed BWB is suitable for up to 250 passengers, a route length of 7,400 nautical miles, and a cruise speed of Mach 0.85. Its large planform area and long-haul route range provide extended passenger comfort and make it a direct competitor for full-service carriers (FSCs). Due to the nontraditional aircraft structure and Code E airport infrastructure restrictions on wingspan, careful preliminary design is followed by constraint-based optimization to create an efficient design. Sections 3 and 4 present the aircraft design at a high level, covering initial sizing and design optimization. Sections 5 through 10 then examine each subsystem in detail, addressing the cockpit and cabin layout, aerodynamic performance, propulsion system, weight buildup, structural configuration, and static and dynamic stability, respectively.

Additionally, several inherent challenges to the BWB platform are addressed in this paper. Due to the lack of horizontal stabilizers from drag penalties, a dual inclined vertical stabilizer system with wing-mounted elevons is integrated with a fly-by-wire active control system to maintain control authority across the flight envelope. Twin high-bypass turbofan engines are aft-mounted to maximize boundary layer ingestion and mitigate yaw instabilities arising during engine-out conditions.

1.2 Technical Drawing

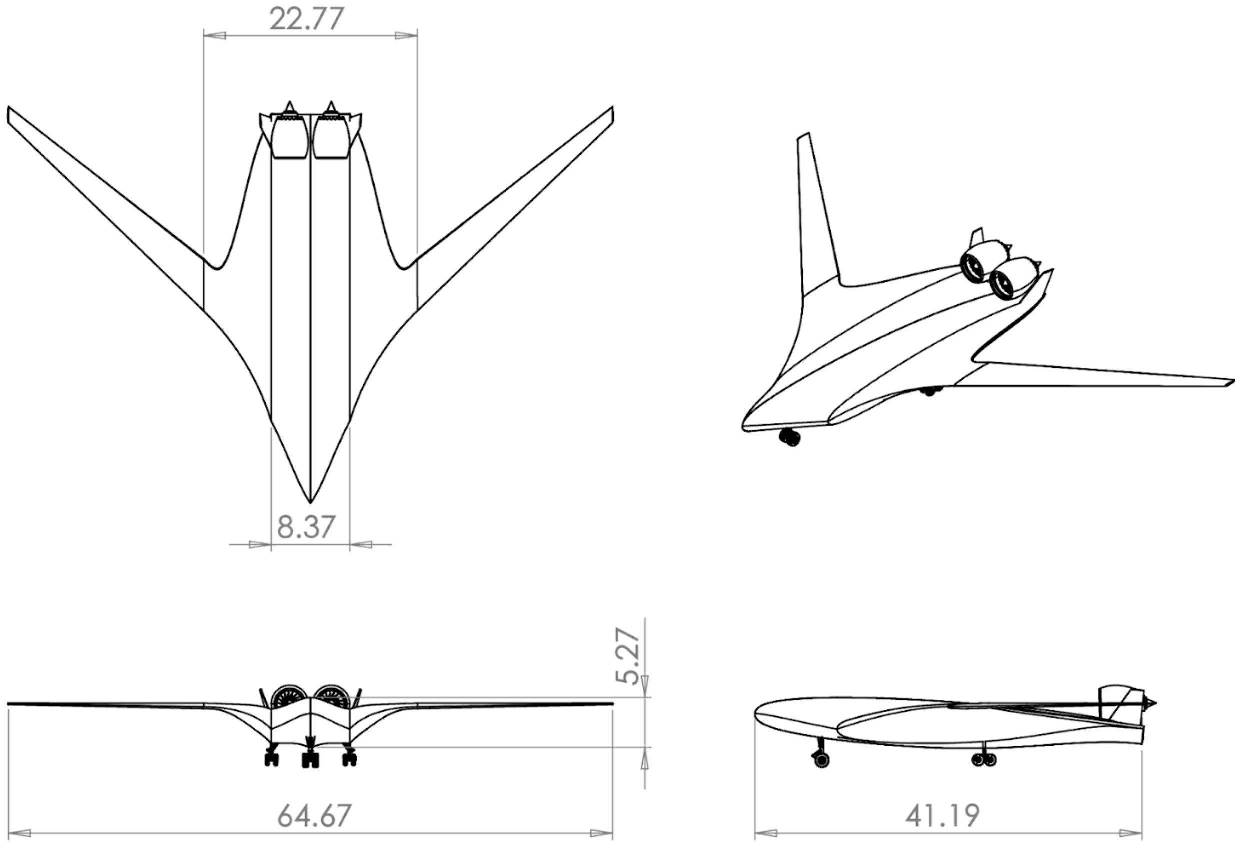

Figure 1: Computer-Aided Design drawing of conceptual BWB Aircraft.

2. Introduction

2.1 Reference Aircraft

The main challenge of designing widebody airliners is to ensure seamless integration into airport gate infrastructure with a span limit of 65 meters. As such, the Boeing 787-8 and JetZero's Z4 were selected as primary benchmarks to evaluate against. The 787-8 dominates the long-haul market with its competitive fuel efficiency and luxurious passenger comfort, while the Z4 is the leading proposal for a BWB airliner. Both of these aircraft guide key design choices and trade studies for initial sizing.

2.2 Critical Technologies

Several technologies are implemented to realize the blended wing body design. Advanced structural composites with high strength-to-weight ratios are integrated in the airframe to allow for large non-circular pressurized cabin vessels. Boundary layer ingestion through aft-mounted high-bypass turbofan engines is utilized to minimize nacelle drag and approach optimal propulsion efficiencies. Novel fuselage design further improves aerodynamic efficiency and ensures stability in combination with a robust fly-by-wire (FBW) active control system.

2.3 Concept of Operations

The BWB is designed for FSCs to service long-haul routes up to 7,400 nautical miles. The presented aircraft is sized for a mission profile from Los Angeles (LAX) to Dubai (DXB), serving two of the major airport hubs around the world. The widebody profile enables FSCs to offer passengers additional premium comfort instead of traditionally capitalizing on dense seating capacities. A baseline flight altitude of 40,000 ft is chosen to optimize fuel efficiency for the maximum loaded payload.

3. Initial Sizing

Empirical data for reference aircraft are used in combination with Raymer's estimation guidelines to determine initial payload, empty weight fractions, and energy storage weight fractions [R2]. The Jet Transport class, as defined in Raymer, best approximates conservative weight estimations for BWBs, despite most of the class containing conventional TAW designs. John T. Hwang's gross weight Marimo notebook is modified to include additional fuel penalties for 30 minutes of loiter and 45 minutes of potential diversion after attempted landing. The resulting weight fractions are shown in Table 2, corresponding to the inputs specified in Appendix A1.

Estimates for wing loading and thrust to weight are required to size the initial propulsion and wing area requirements for the proposed BWB. A constraint analysis is performed subject to a five percent safety margin to ensure preliminary stall, climb, maneuver (approach and cruise), takeoff, landing, and ceiling constraints are satisfied. John T. Hwang's sizing carpet plot Marimo notebook is utilized to generate the carpet plot shown in Appendix A3, with input parameters displayed in Appendix A2.

Table 2: Estimated gross, payload, empty, and energy storage weight fractions, combined with estimated wing loading and thrust-to-weight used for initial aircraft sizing.

Gross Weight [N]	**Payload Wt Frac.**	**Empty Wt Frac.**	**Energy Storage Frac.**	**W/S [N/m^2, lb/ft^2]**	**T/W**
1,707,300	0.23	0.41	0.36	3683, 80.5	0.42

4. Design Optimization and Sensitivity Analysis

4.1 Master Script

A *Master Script* is created to integrate individual computations into one sequential script, minimizing time spent during geometry creation and design refinement and eliminating inconsistent input parameters across evaluations. The tool takes advantage of OpenVSP, a NASA open source parametric geometry toolkit, and AVL, an MIT-developed extended vortex lattice model, to automatically generate the blended wing body geometry and evaluate key aerodynamic performance parameters across the flight envelope. OpenVSP is utilized for the computation of aircraft wetted area, parasitic drag coefficient, and mean aerodynamic chord (MAC), in addition to visualizing the aircraft's current configuration. AVL enables accurate determination of the aircraft's neutral point (Np) during transonic cruise conditions and computes normalized resulting moments across surfaces for constraint validation. Additionally, estimations of mission-level weight fractions, individual component weights, center of gravity (CG), aerodynamic efficiencies, structural stress, and cost are integrated into the Master Script to enable rapid design evaluation. A set of four design parameters and mission objectives are used to streamline the design process, enabling efficient parameterization by segmenting the plane into three reflected sections.

Table 3: Design parameters and mission objective inputs.

Design Parameters	AR [1x4]	Sweep [1x4]	Area [1x4]	Taper Ratio [1x4]
Mission Objectives	Range	Mach	Altitude	Payload

4.2 Gradient-Free Optimization

While tools like OpenVSP and AVL simplify the evaluation of candidate designs, their lack of explicit derivative information limits the use of gradient-based optimization. As such, gradient-free Particle Swarm Optimization (PSO) is implemented to determine the set of design parameters that maximize aerodynamic efficiency.

Design variables:

$$\mathbf{x} = [\mathbf{AR},\, \mathbf{S},\, \boldsymbol{\lambda},\, \boldsymbol{\Lambda}]; \qquad \mathbf{AR},\, \mathbf{S},\, \boldsymbol{\lambda},\, \boldsymbol{\Lambda} \in \mathbb{R}^3$$

Objective:

$$\max_{\mathbf{x}} \ \frac{L}{D}(\mathbf{x})$$

Constraints:

$$\sigma(\mathbf{x}) \leq \sigma_{\text{allow}}, \qquad SM(\mathbf{x}) \geq 0$$

Bounds:

$$[\mathbf{AR}_{\text{min}},\, \mathbf{S}_{\text{min}},\, \boldsymbol{\lambda}_{\text{min}},\, \boldsymbol{\Lambda}_{\text{min}}] \leq \mathbf{x} \leq [\mathbf{AR}_{\text{max}},\, \mathbf{S}_{\text{max}},\, \boldsymbol{\lambda}_{\text{max}},\, \boldsymbol{\Lambda}_{\text{max}}]$$

This algorithm explores the design space by randomly generating candidate solutions, called *particles*, and assigning each position a score based on the objective function. Across numerous iterations, particles gradually converge toward an optimal solution by weighing their own best-known position against the best position discovered by their neighbors. This particular problem employs a global-best topology structure, where a particle's neighborhood includes the entire swarm. It excels over other methods for its fast convergence in low-dimensional problems with high computational cost per design evaluation. The control parameters corresponding to cognitive, social, and inertial behavior are set to one, two, and 0.5, respectively, to prioritize particle motion toward the swarm's global best. Implementation of the algorithm is handled using the Python PySwarms library.

The optimization problem is formulated to maximize the aircraft's lift-to-drag ratio while satisfying constraints on allowable material stress (Section 9.1), positive static margin (SM) (Section 10.1), Class E wingspan restrictions, and bounds on wing design parameters (Sections 5.2, 6.2). To map the design space and establish a performance baseline, the solver is first run with a swarm of 40 particles for 25 iterations. PSO is then run iteratively by establishing new bounds within ±20% of the previous design for further refinement. This approach serves as a robust alternative to performing a single large-scale optimization, conserving computational power by limiting particle count, and exploring the design space in batches.

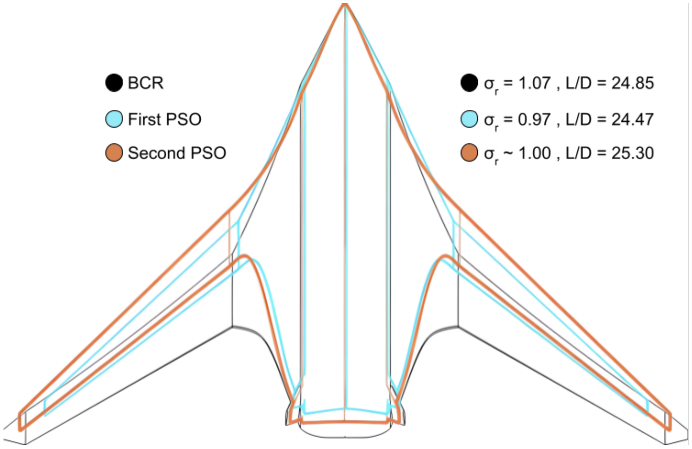

Figure 2: Optimized BWB geometries from the first PSO run (cyan) and second PSO run (orange), overlaid on the initial design (black). The two PSO runs improved L/D from 24.85 to 25.30 while driving the stress ratio to its constraint limit.

4.3 Sensitivity Analysis (Monte Carlo)

A large-scale sensitivity analysis is performed using a Monte Carlo simulation to assess how variations in key parameters influence the design's performance. Each design parameter is varied by ±40%, subject to geometry constraints defined in Section 4.2. Instead of using a traditional random sampling approach to simulate $N = 1{,}000$ designs, Latin Hypercube sampling is implemented to evaluate the full design space, where the cumulative distribution function of each design parameter is discretized into N equally probable intervals, significantly reducing the number of simulations needed. For the purpose of evaluating trends local to the optimized design, all four mission objective parameters are held constant.

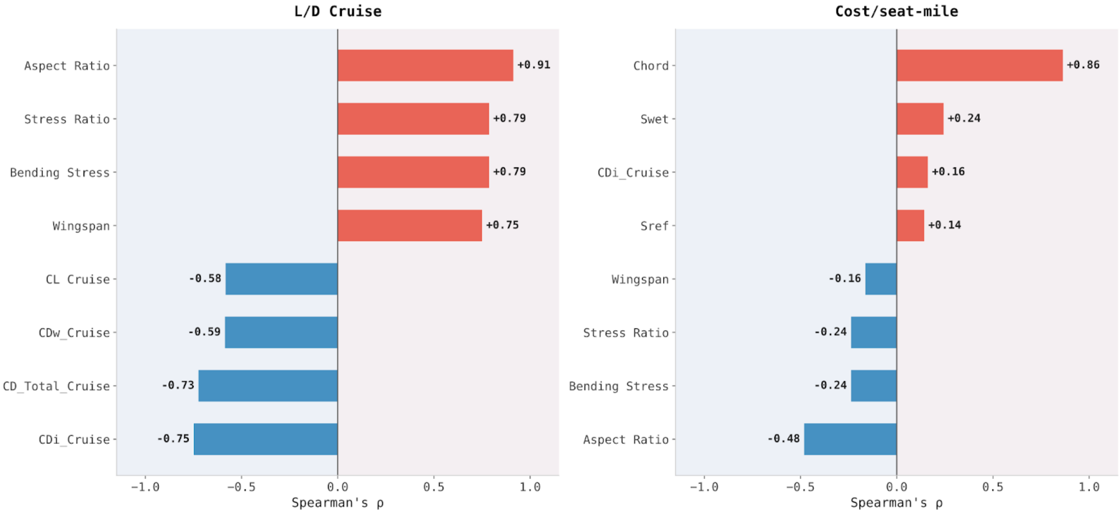

Figure 3: Major influences of design space parameters on (a) cruise efficiency and (b) cost/seat-mile.

The Spearman rank correlation indicates that aspect ratio has the greatest influence on L/D Cruise, while chord length most strongly affects cost per seat mile (Figure 3). Additionally, a full matrix correlation heatmap is included in Appendix A9. These figures significantly motivate the modifications from BCR to CoDR, and help validate gradient-free optimization design choices.

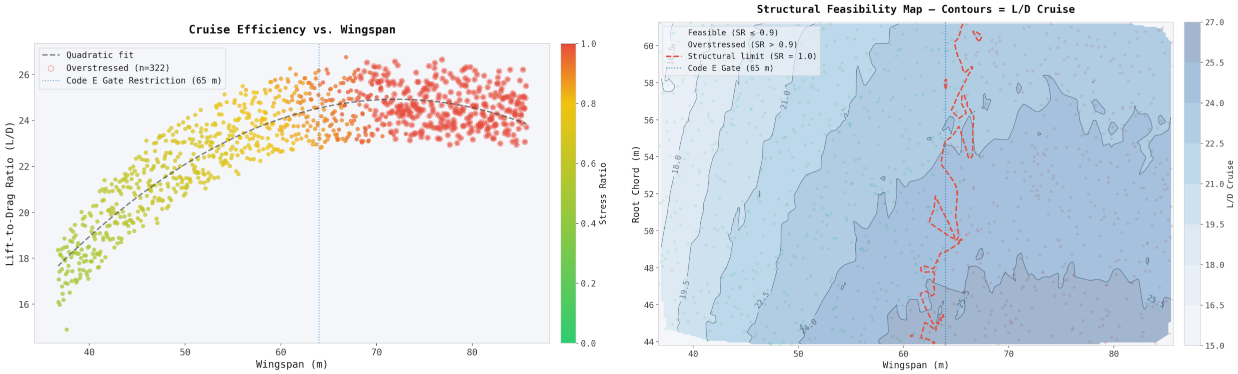

Figure 4: (a) Pareto plot between cruise efficiency and wingspan. (b) 2-D design space projection subject to structural constraints and objective contours (cruise efficiency).

Design optimization analysis highlights the tradeoff between cruise efficiency and material allowables, particularly indicating the potential for overstressed configurations to begin occurring at less than 65 m during optimal lift-to-drag ratios (Figure 4). This validates our sub Gate E wingspan computed through gradient-free optimization, removing the need for further investigations into folding wing designs.

5. Concept

5.1 Passenger and Cargo Configuration

The proposed BWB aircraft concept adopts a triple-aisle main cabin configuration, maximizing high-capacity long-range operability and passenger comfort. The first class cabin is configured in the triangular front section of the airframe, with 20 luxury seats. The triangular planform allows for premium lavatories and additional space to accommodate a shower or meeting room, subject to airline requirements. The main cabin, composed of three rows of business seats and 16 rows of economy seats, incorporates a 2-4-4-2 seating arrangement to balance passenger comfort and evacuation regulations. Two sets of floor-level exits are available to provide sufficient evacuation routes for passengers during emergencies. Designated cabin crew quarters are placed underneath the first class section. Flexible cargo space exists on both sides of the main cabin, as well as beneath it, to provide ample LD-3 containers to house standard passenger loads and additional goods.

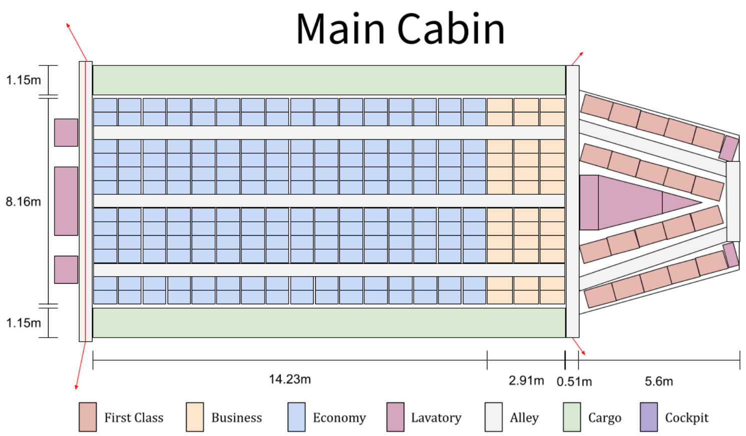

Figure 5: Proposed BWB main cabin configuration detailing the 2-4-4-2 seating arrangement.

5.2 Fuselage Design

The fuselage is sized to meet cabin layout requirements while supporting aerodynamic efficiency. Minimum spanwise dimensions are established from the fuselage outward, including an additional buffer of 1.75 inches according to industry standards. The minimum fuselage length is determined by assuming that the rear of the pressurized cabin is at 70% of the root chord to handle bending and shear loads from the outer wing section [R2]. Following the calculations outlined in Appendix A4, the minimum fuselage length is 39 m. Accounting for 2% insulation requirements on the cabin width, as well as space added from adjacent cargo, the minimum fuselage width is calculated to be 10.71 m. Cabin height is determined to be 5.27 m using the fuselage length and the thickness-to-chord ratio of the NACA 25111 airfoil. These dimensions establish bounds on PSO design variables to ensure that the algorithm only explores geometrically feasible configurations.

5.3 Nose and Landing Gear Design

A multi-bogey landing gear system is selected to satisfy ground clearance requirements while maximizing rotation capability. The system consists of three retractable struts near the midpoint of the aircraft. The main landing gear consists of four wheels, while the nose gear features a pivoting two-wheel design. Conducting a CG excursion analysis with respect to fuel burn, the aircraft's CG is determined to vary between 22.7 and 19.9 m aft of the nose. Applying the 15° clearance criterion [R3], the landing and nose gear are placed 24.2 m and 8.2 m aft of the nose, respectively, to ensure adequate rotation ability. The two side struts adjacent to the landing gear are offset by 3.2 m from the centerline and 22.7 m from the nose. In this configuration, the static configuration load fraction reaches a maximum of 14.6% across all loading cases, lying in between the recommended range of 5%–20% for transport aviation [R3].

The potential rotational strike zone is examined to determine the required landing gear height during takeoff and landing. To ensure safety, a maximum rotation angle of 12.1° and a clearance margin of 0.5 m are selected to account for off-nominal strut compression or runway irregularities [R4]. As a result, the landing gear height is determined to be 3.3 m. Finally, wheel sizing is performed to ensure the main landing gear is capable of supporting the majority (85.4%) of the aircraft's weight. Based on empirical transport category correlations, tire diameter and width are estimated to be 0.9 m and 0.3 m respectively [R3].

6. Aerodynamics

6.1 Airfoil Selection

The proposed BWB concept is divided into two distinct airfoils to simplify aerodynamic design. The center body houses passengers, cargo, and primary structural elements, while the outer wing houses fuel tanks and control surfaces. Center body airfoil selection prioritizes maximizing the lift-to-drag ratio at cruise conditions. The NACA 25111 airfoil is well-suited for this purpose, producing the highest lift coefficient among airfoils that can smoothly integrate into the BWB architecture [R5]. Outer wing airfoil selection focuses on reducing transonic drag effects and minimizing instabilities. The NASA SC(2)-0410 airfoil is chosen for its 10% thickness-to-chord ratio, which maintains a balance between structural integrity and drag reduction across the flight regime. However, the airfoil produces a large negative moment coefficient, motivating the implementation of an active fly-by-wire control system (Section 10.2).

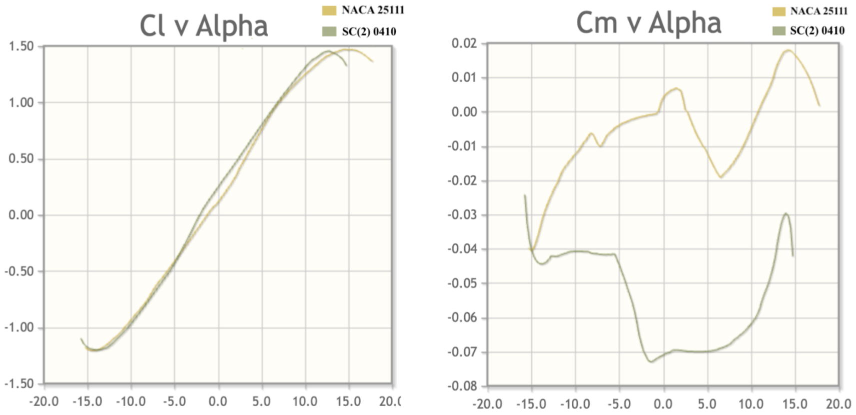

Figure 6: NACA 25111 and NASA SC(2)-0410 changes in (a) Lift Coefficient and (b) Moment Coefficient across varying angles of attack from ±20°.

6.2 Wing Design

Outer wing dimensions are constrained by compliance with Code E gate restrictions (Section 2.1), with a maximum allowable wingspan of 65 m. Sweep angles are limited to a maximum of 65°, consistent with studies on BWB planform design showing diminishing aerodynamic efficiency and structural penalties at high sweep angles [R6]. These wing bounds help define a design space for the optimization problem, along with fuselage and structural constraints, driving the PSO algorithm towards a feasible optimized wing geometry. Optimized airfoil design parameters are summarized in Appendix A7.

6.3 Lift and Drag Analysis

Lift and drag analysis is conducted by discretizing the wing into three representative airfoil regions and summing sectional properties to derive spanwise aerodynamic parameters. For a Reynolds number on the order of 10^8 and a transonic Mach number of 0.85, sectional lift coefficients are calculated using equations detailed in the aerodynamics section of Raymer [R3] and airfoil geometry parameters (Section 6.2). Sectional lift curves are corrected to account for sweep, aspect ratio, and compressibility effects and combined using an area-weighted summation to obtain the total lift coefficient. The overall drag coefficient is formed as the sum of parasite, wave, and lift-induced drag contributions from each section using similar empirical relations derived in Raymer.

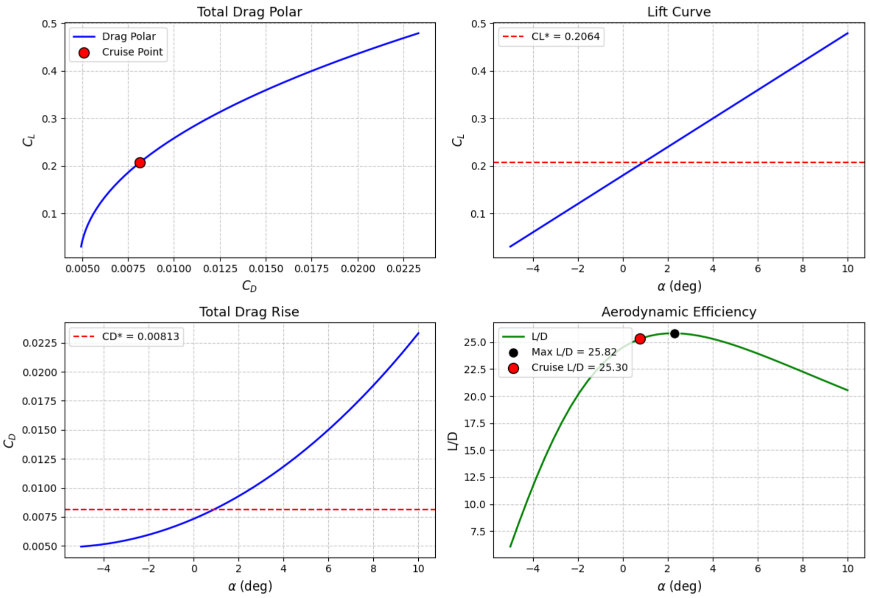

Figure 7: Top left to bottom right: Total Drag Polar (C_L vs. C_D); Lift Curve vs. AoA; Total Drag Rise; Aerodynamic Efficiency (L/D) vs. AoA.

Table 4: Aerodynamic parameters at a 0.896° angle of attack during cruise.

C_L	AoA (°)	$C_{D,0}$	$C_{D,i}$	$C_{D,w}$	C_D	L/D	$\frac{dC_L}{d\alpha}$ (π)
0.21	0.896	0.0049	0.0029	0.0003	0.0081	25.3	1.71

7. Propulsion

7.1 System Architecture and Integration

The proposed BWB employs a twin-engine configuration consisting of GEnX-1B high-bypass turbofan engines mounted on the upper aft surface of the airframe. This system architecture is selected to maximize propulsion efficiency and integration feasibility while using available technologies. Mounting the engines at the rear reduces aerodynamic interference with the primary lifting surfaces and enables boundary layer ingestion (BLI) of low-energy flow along the upper airframe surface. BLI is maximized by smoothly integrating the nacelles into the airframe, reducing nacelle drag and lowering the inlet velocity. Upper-surface mounting allows for airframe acoustic shielding, reducing noise while minimizing ground clearance and foreign object damage risks during ground operations. Engines are structurally integrated into the airframe using internal reinforced spars for efficient management of engine loads.

Table 5: Key propulsion system parameters for the BWB aircraft with a GEnX-1B engine [R7].

TSFC (1/s)	Bypass Ratio	Weight (N)	Thrust (N)	Mass Flow (kg/s)	Inlet Diam. (m)	Pressure Ratio	Count
1.415×10^{-5}	9.1	62,264	330,000	1160	2.82	43.7	2

7.2 Component Selection and Sizing

The GEnX-1B turbofan engine is selected due to its high-bypass ratio and proven long-haul operability. This engine satisfies all of the aircraft's maneuver requirements (takeoff, climb, loitering, and landing) while upholding engine-out safety margins, providing a maximum takeoff thrust of 330 kN. The high-bypass ratio results in lower specific fuel consumption and maximizes total efficiency. This concept utilizes currently available technologies to minimize this program's time spent in development, testing, certification, and manufacturing.

8. Weight Distribution

An aggregate weight breakdown is conducted using equations presented in Raymer's Chapter 15.3.3 [R3]. As these relations are derived from conventional TAW aircraft, they serve as first-order approximations for the BWB configuration. An iterative method for determining the BWB's MTOW and component weights is implemented subject to the estimated weight fraction (Section 3). The method is chosen due to its robustness to initial guesses varying several orders of magnitude. The full breakdown is shown in Appendix A5.

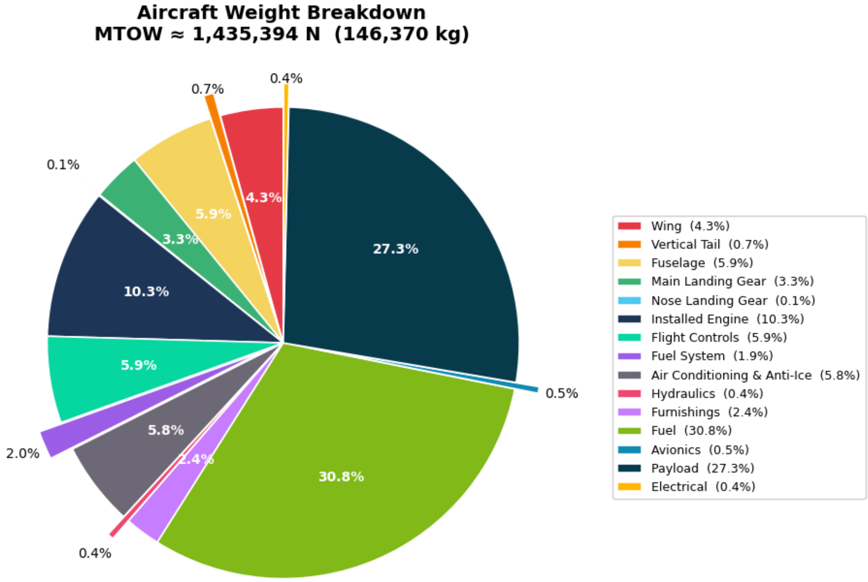

Figure 8: The individual component weight contributions for the proposed BWB design.

9. Structures and Materials

9.1 Overall Structural Layout

Material Selection is driven by the objective of achieving maximum fuel efficiency. This requires structural weight reduction without sacrifices in durability and manufacturability for commercial service. The primary lifting structures, notably the centerbody and wings, are made of Carbon Fiber Reinforced Polymer (CFRP), while keel and I-beams supporting structures are made of High Modulus Carbon Fiber. This is primarily due to carbon fiber's high specific strength and stiffness, enabling a significant reduction in empty weight compared to metallic structures. Aluminum is selected for the wing and tail ribs to ease manufacturability and reduce unnecessary costs. Titanium is selected for design in high-temperature and high-load environments such as engine mounts and wing-body transition sections, due to its high strength and operating temperature. Steel is reserved for landing gear components where fatigue resistance and strength are essential. Metallic reinforcements made of Titanium and Aluminum are incorporated into impact-prone areas like leading edges to improve damage tolerance. This combination of materials minimizes structural weight while emphasizing safety and longevity in our design.

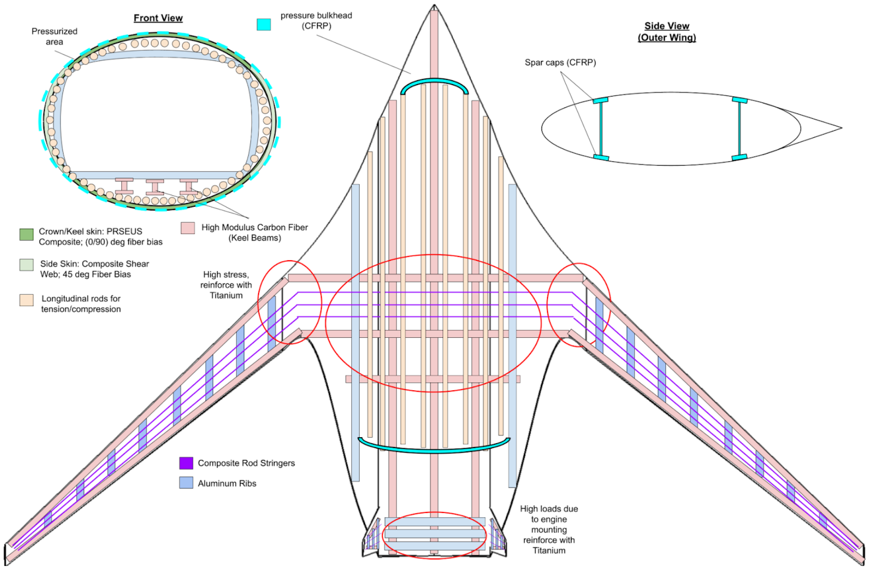

Figure 9: Preliminary structural layout of the baseline BWB configuration. Top left: Front view from the nose. Top right: Side view of the central body. Middle: Top-down view.

Structural integrity is evaluated by comparing estimated maximum stresses (σ) to the ultimate strength of CFRP [R8] using a factor of safety of 1.5. The main contribution to wing root stress is assumed to be longitudinal bending from aerodynamic loads to provide a simplified metric for structural assessment. Calculating stress values starts with obtaining root bending moments (M) from AVL for each of the three planform sections. Using standard beam theory, these moments are applied to a simplified spar cap model to estimate stress, where the maximum bending stress is:

$$\sigma_i = \frac{M_i\, y_i}{I}$$

The moment of inertia (I) is estimated as $I = 4A\, y_i^2$ using the parallel axis theorem, assuming four spar caps located a distance y_i from the neutral axis act as the primary load-carrying elements with negligible individual moments of inertia. Structural design parameters are summarized in Appendix A8.

9.2 Fuselage Structural Design

The proposed BWB fuselage outperforms conventional TAW aircraft designs by maximizing aerodynamic efficiency gains from the central lifting body. However, its elongated elliptical shape leads to an asymmetric distribution of internal pressurization. Pultruded Rod Stitched Efficient Unitized Structures (PRSEUS) offers a viable solution to this challenge. This technology lines the inside of the skin to increase the body's resistance to buckling by distributing axial loads efficiently. In combination with stiffened shell panels, these rods prevent structural collapse during yielding, reducing the impact of pressurization and aerodynamic loads on the BWB's structural integrity.

9.3 V-n Diagram

The V-n diagram is used in this study to define the structural load envelope for the proposed BWB aircraft across the flight envelope. Gust conditions were evaluated with respect to Federal Aviation Regulation part 25, and have minimal impact on the loading conditions during flight due to the BWB's large planform area. The resulting envelope is consistent with transport class limits.

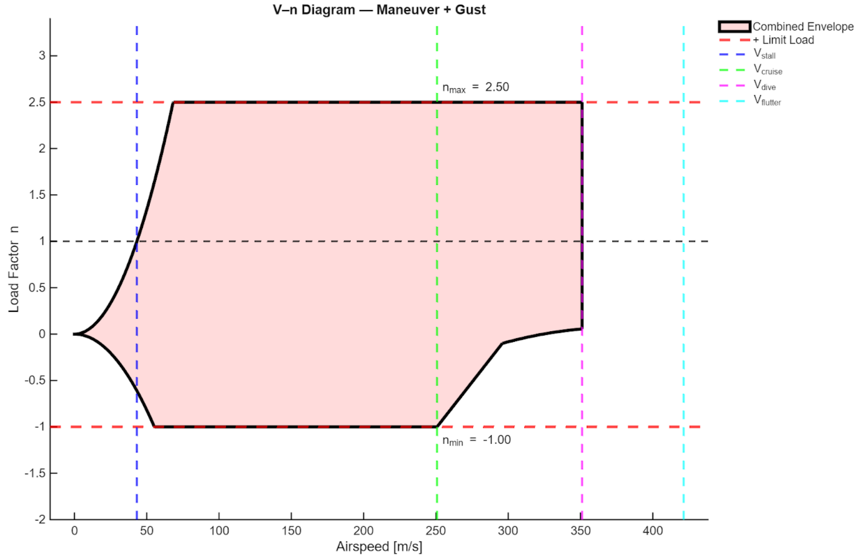

Figure 10: V-n diagram showcasing the load factor n versus airspeed for various mission phases.

10. Stability and Controls

10.1 Static Stability

To evaluate static stability, the Np, longitudinal CG, and SM are computed throughout our design mission. A table of resulting parameters is below.

Table 6: Key longitudinal stability parameters for the proposed BWB configuration at MTOW.

Parameter	**Np**	**CG**	**SM**
Meters, % MAC	24.6, 101	22.7, 92.8	N/A, 7.8

The neutral point is found through two methods: (i) a direct computation from AVL during the nominal cruise condition, or (ii) a fallback empirical method based on airfoil properties and planform geometry. The longitudinal CG of the aircraft is determined by aggregating the individual contributions of the heaviest components, with their respective CG locations (Figure 11a). A CG excursion analysis is used to determine the variance in SM throughout flight (Section 5.3). The SM is computed as a percentage of the MAC using $Np - CG/MAC = SM$. Compared to TAW designs, the SM of the BWB increases as fuel is burned due to aft fuel CG.

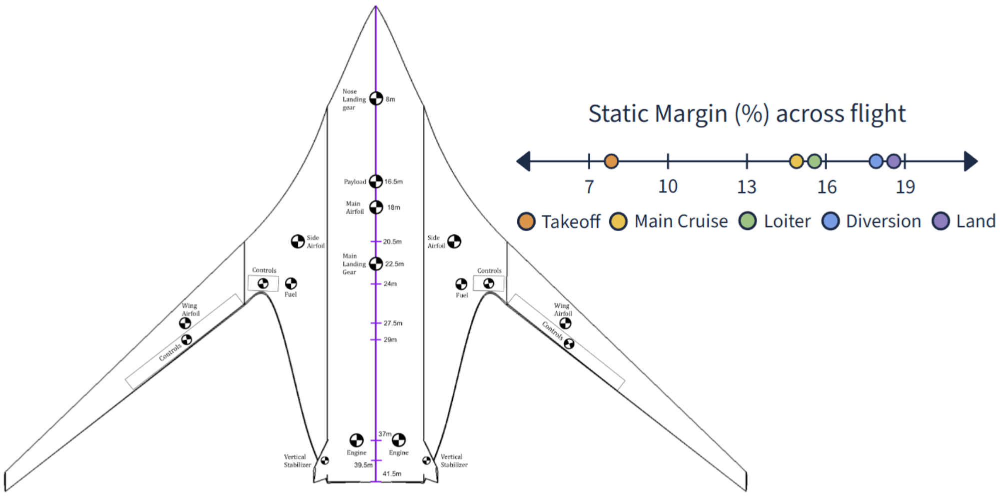

Figure 11: (a) Nose-relative CG of major components and (b) SM during mission phases.

10.2 Dynamic Stability

BWBs pose inherent challenges to achieving passive lateral stability due to the use of supercritical reflex airfoils and small stabilizer moment arms. Implementing twin inclined vertical stabilizers can help mitigate this instability, but is insufficient during cruise conditions due to the overpowering contributions from the reflexed center body. As such, a digital FBW active control system must be implemented to ensure stability across the flight envelope.

To evaluate the inherent dynamic stability of the aircraft in its current configuration, a state-space model is developed from work done by Etkin and Reid [R9]. The state matrix is developed using stability derivatives at nominal cruise conditions derived from AVL and 3-axis moments of inertia computed from the major component masses and their locations. Through an eigenvalue analysis for longitudinal stability, the rise, settling time, and damping ratios are obtained and compared to standard acceptance levels laid out by Sadraey M.H. [R10].

Table 7: Longitudinal dynamic stability parameters for the short period and phugoid modes.

Mode	**Eigenvalues**	**Damping Ratio**	**Time to Double [s]**	**Acceptance Level**
Short period	$-0.5473 \pm 1.71i$	0.303	—	2
Phugoid	$0.0012 \pm 0.0367i$	−0.0314	600	3

The small negative damping ratio of the phugoid mode indicates that the aircraft's oscillations will grow slowly with time, requiring the pilot to constantly correct this behavior (Table **??**). Additionally, the dynamic stability acceptance levels indicate the need for higher pitch authority to steer the aircraft back to equilibrium after a pitch disturbance, motivating the implementation of a FBW control system.

Table 8: Lateral dynamic stability key parameters without FBW implementation.

Mode	**Eigenvalues**	**Time Constant [1/s]**	**Damping Ratio**	$t_{1/2}/t_{\textbf{double}}$ **[s]**	**Accept. Level**
Roll subsidence	−0.58	1.72	1	0.52	2
Spiral divergence	0.074	13.3	−1	4.06	3
Dutch roll	$-0.036 \pm 0.83i$	27.8	0.043	8.36	2

With acceptance levels greater than two, the lateral stability characteristics of the proposed design put excessive strain on the pilots and are unsustainable for long-haul flight missions (Table **??**). This motivates the implementation of a FBW active control system to compensate for the absence of long, coupled control surfaces and stabilizers found on conventional TAW aircraft. The FBW system uses rapid feedback loops to interface between pilot input, airplane dynamics, and flight disturbances.

The proposed FBW control system is based on the system built for the Boeing X-48 – a pioneer in practical FBW implementation. The system consists of independent pitch, yaw, and roll augmentation control systems that are later merged by a master control system, analogous to the X-48's LSCAS, RSCAS, and DSCAS control systems [R12]. Potential risks of this system include loss of redundancy, robust control ability, and pilot control, which have precluded it from being implemented as the central control system for commercial aircraft. However, the proposed FBW control system incorporates a triplex flight control computer system, which has the capability of overriding commands that may be corrupted. The control system's robustness will be evaluated using extensive modelling and flight testing before final production.

11. Cost Analysis

11.1 Direct Operating Cost and Cost per Flying Hour

Aircraft operating cost is a primary metric for evaluating economic performance during normal operations. Total direct operating cost (DOC) is calculated by aggregating costs associated with the typical mission profile, including fuel consumption, crew salaries, maintenance, fees, and depreciation [R3]. Based on these calculations, the DOC comes to \$12,237 per flight hour, corresponding to a cost per available seat mile (CASM) of \$0.0873. This value is lower than the typical CASM values for many existing commercial aircraft, which range between \$0.09–\$0.15 per seat-mile [R13], and translates to a total operating cost of ∼\$187,000 for a full flight from Los Angeles (LAX) to Dubai (DXB). The component cost breakdown shows that fuel represents the largest operating expense at approximately 34%, followed by maintenance materials at 28% (Figure 12). These results are consistent with commercial aircraft cost distributions, where fuel and maintenance dominate total expenses. Overall, the DOC and CASM lie within a range that validates the feasibility of the proposed design.

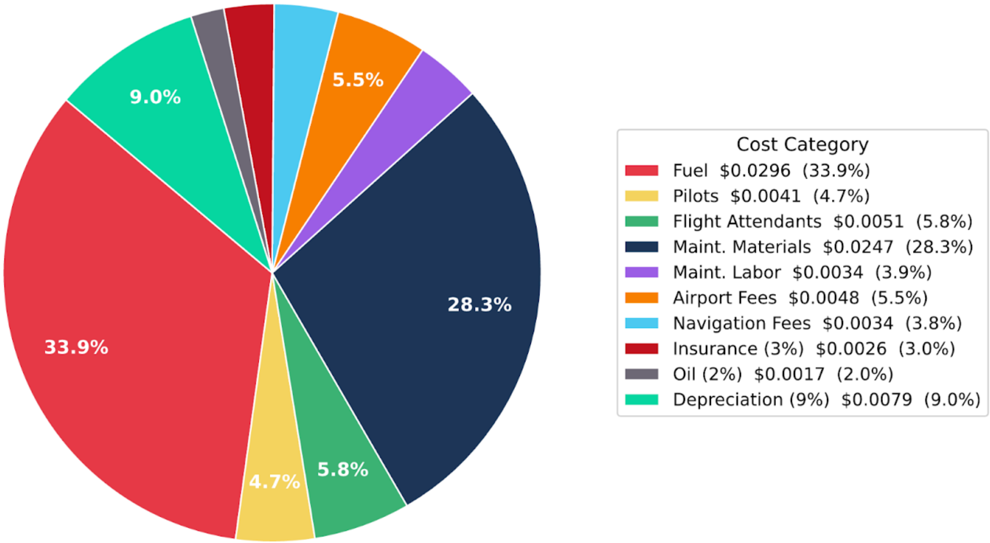

Figure 12: Direct Operating Cost (DOC) CASM breakdown of the proposed BWB.

11.2 Break-Even Analysis

A cost analysis for the aircraft design is conducted to determine economic viability. This analysis includes both recurring flyaway costs (maintenance and manufacturing, fuel, avionics, etc.) and initial Research, Development, Testing & Evaluation (RDT&E) costs [R3]. The price of each aircraft is set to 1.4 times the cost of production to recuperate RDT&E costs.

The cost analysis indicates that all development costs are recouped at the break-even point of 249 aircraft sold (Figure 13a), after which sales result in net profit. A time-value of money analysis is conducted to determine the number of years needed to break-even. Using predictions of future inflation, return rates, and reinvested earnings, this analysis indicates that it will take 20 years to reach the break-even point (Figure 13b).

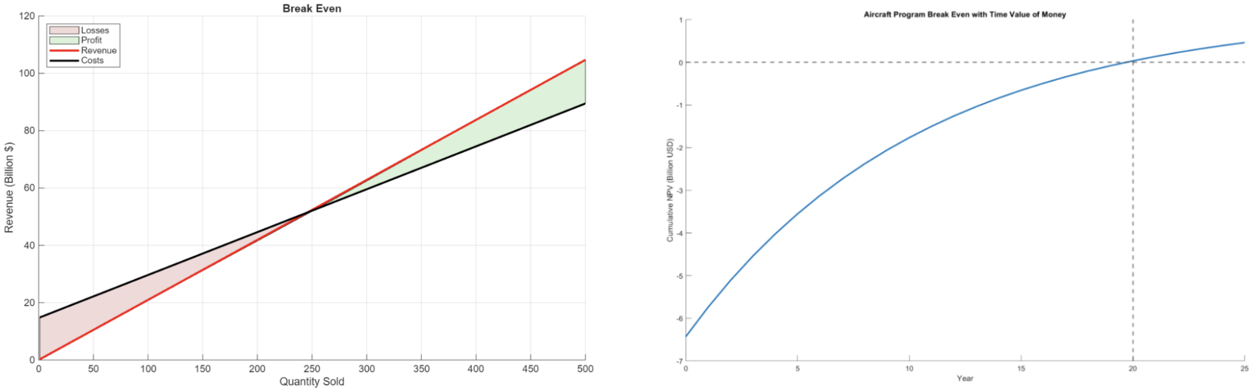

Figure 13: (a) Break-Even Chart and (b) Cumulative Net Present Value Plot

References

[1] International Council on Clean Transportation (ICCT). *CO_2 emissions from commercial aviation, 2018.* 2019.

[2] Nickol, C. L., & McCullers, L. A. *A sizing methodology for the conceptual design of blended-wing-body transports.*

[3] Raymer, D. P. *Aircraft Design: A Conceptual Approach*, 6th ed. AIAA, Reston, VA, 2018.

[4] NASA. *Refined exploration of turbofan design options for an advanced single-aisle transport aircraft.*

[5] Baig, A. Z., et al. "A New Methodology for Aerodynamic Design and Analysis of a Small Scale Blended Wing Body." *Journal of Aeronautics & Aerospace Engineering*, 7(1), 2018. https://doi.org/10.4172/2168-9792.1000206

[6] Ali, U., Okasha, M., Dief, T. N., ElSayed, M. S. A., & Kamra, M. M. "Blended wing body designs for aerodynamic, stability, and control optimisation: A comprehensive review." *Transportation Engineering*, 22, 100397, 2025.

[7] GE Aerospace. "GenX Engine." www.geaerospace.com/commercial/aircraft-engines/genx.

[8] Bekdaş, G., et al. "Optimum CFRP Design for Flexural Strengthening of Cantilever Concrete Walls Using Artificial Neural Networks." *Polymers*, 17(24), 2025.

[9] Etkin, B., & Reid, L. D. *Dynamics of Flight: Stability and Control*, 3rd ed. John Wiley & Sons, 1995.

[10] Sadraey, M. H. *Aircraft Design: A Systems Engineering Approach.* John Wiley & Sons, 2012.

[11] Liebeck, R. H. *Beyond tube-and-wing: The X-48 blended wing-body and NASA's quest to reshape future transport aircraft.*

[12] Liebeck, R. H., Page, M. A., and Rawdon, B. K. "Blended-Wing-Body Subsonic Commercial Transport." AIAA Paper 98-0438, 1998.

[13] American Airlines. *American Airlines Reports Fourth-Quarter and Full-Year 2024.*

Appendices

A1: Initial Sizing — Weight Fraction Input Parameters

Parameter	**Value**
Aircraft type	Jet-propelled
Empty weight fraction coefficient, a	0.97
Empty weight fraction exponent, b	-0.06
Payload weight, W_p [N]	392,000
Range, R [m]	1.3705×10^7
Cruise speed, V [m/s]	250.7
Lift-to-drag ratio, L/D	22.5
TSFC, c_T [kg/N/s]	1.415×10^{-5}
BSFC, c_P [kg·s/W]	5×10^{-8}
Efficiency, shaft to thrust power, η_j	0.9
Efficiency, battery to thrust power, η_b	0.9
Battery specific energy, e_b [J/kg]	7×10^5
Battery specific energy, e_k [J/kg]	4.4×10^7
Loiter time, t_l [min]	30
Additional cruise time, t_c [min]	45

A2: Initial Sizing — Wing Loading and Thrust-to-Weight Input Parameters

Parameter	**Value**
Cruise speed, V_{cruise} [m/s]	250.7
Climb speed, V_{climb} [m/s]	73.56
Stall speed, V_{stall} [m/s]	61.3
Takeoff speed, V_{takeoff} [m/s]	67.43
Approach speed, V_{approach} [m/s]	79.7
Cruise altitude, h_{cruise} [m]	12,192
Parasitic drag coeff., C_{D0i}	0.0078
Max. lift coeff., $C_{L\,\text{max}}$	1.7
Takeoff lift coeff., $C_{L_{\text{takeoff}}}$	1.485
Manoeuvre load factor, n	2.5
Climb angle, γ [deg]	2.7
Oswald efficiency factor, e	0.85
Aspect ratio, AR	12
Thrust Mach lapse, k	0.4
Thrust density lapse, m	0.7
Takeoff density altitude, h_{takeoff} [m]	1609
Landing density altitude, h_{landing} [m]	1609
Takeoff parameter coefficient, k_{takeoff} [m^3/N]	0.255
Landing parameter coefficient, k_{landing} [m^3/N]	0.51
Landing distance, d_{landing} [m]	1905
Airborne distance, d_{airborne} [m]	300
Takeoff distance, d_{takeoff} [m]	3352.8

A3: Initial Sizing — Wing Loading and Thrust-to-Weight Carpet Plot

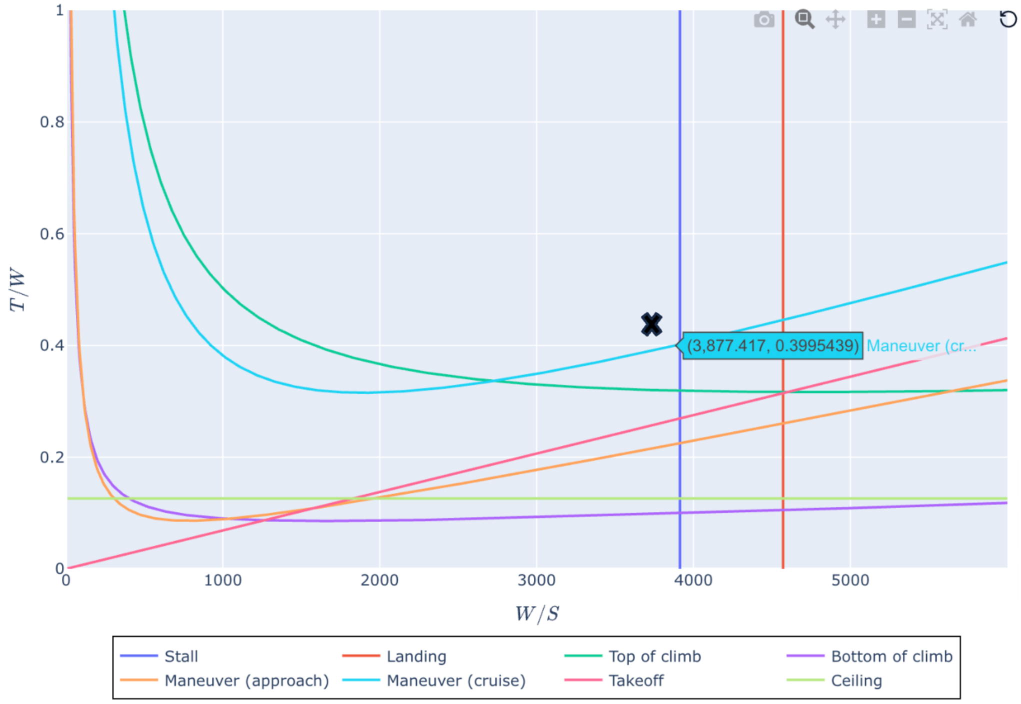

Figure 14: Thrust-to-weight ratio (T/W) versus wing loading (W/S) diagram illustrating key aircraft performance constraints. The black × indicates a 5% safety margin from all constraints.

A4: Initial Sizing — Interior and Exterior Sizing Calculations

Fuselage Width

Component	Dimension
12 Passenger Seats (54 cm/seat)	6.48 m
3 Aisles (51 cm/aisle)	1.53 m
Cargo	2.30 m
R&L Wing Padding	0.15 m
Interior Cabin Width	**10.46 m**
Fuselage + Insulation	0.25 m
Exterior Cabin Width	**10.71 m**

Chord Length

Component	**Dimension**
Main Cabin	17.14 m
Cockpit (statistical)	4.50 m
First Class	6.20 m
Alley (front + back)	1.02 m
Lavatory (front + back)	2.00 m
Interior Cabin Length	**30.86 m**
Fuselage + Insulation	0.66 m
Estimated Exterior Length	31.52 m
Assumption: 70–80% of total chord	—
Chord Length	**39 m**

Fuselage Height

Parameter	**Value**
Centre t/c	11%
Fuselage Height	**4.29 m**

A5: Weights and Sizing

Table 1: Component weight totals and percentages.

Weight Segment	**Weight (N)**	**Weight (%)**
Wing	6.164×10^4	4.294
Vertical Tail	1.010×10^4	0.703
Fuselage	8.419×10^4	5.865
Main Landing Gear	4.775×10^4	3.326
Nose Landing Gear	1.023×10^3	0.071
Installed Engines	1.477×10^5	10.291
Fuel System	2.799×10^4	1.950
Flight Controls	8.520×10^4	5.936
Hydraulics	6.261×10^3	0.436
Avionics	6.479×10^3	0.451
Electrical	5.383×10^3	0.375
Air Conditioning & Anti-Ice	8.262×10^4	5.756
Furnishings	3.469×10^4	2.417
Fuel	4.424×10^5	30.818
Payload	3.920×10^5	27.310
Total	1.435×10^6	100.000

A6: Empirical Aerodynamic Relations

Wave Drag:

$$C_{DW} = 20\,(M - M_{Cr})^4$$

where M is the Mach number and M_{Cr} is the critical Mach number.

$$M_{DD} = \kappa_A - \left(\frac{t}{c}\right) - 0.1\,C_L$$

where M_{DD} is the drag-divergence Mach number, $\kappa_A = 0.95$ for supercritical airfoils, t/c is the thickness-to-chord ratio, and C_L is the lift coefficient.

$$\frac{dC_{DW}}{dM} = 0.1$$

A7: Geometric and Aerodynamic Parameters — Baseline BWB Configuration

Table 2: Geometric and aerodynamic parameters defining the baseline BWB configuration.

Parameter	**Value**
Aspect Ratio	5.03
Total Wing Span (m)	64.67
Fuselage Height (m)	5.27
$S_{\text{wet}}/S_{\text{ref}}$	1.85
LE Sweep — Centre Airfoil (°)	65.00
LE Sweep — Outer Airfoil (°)	43.76
NACA 25111 Airfoil t/c (%)	11
NASA SC(2)-0410 Airfoil t/c (%)	10
NACA 25111 Centre Chord Length (m)	41.19
NACA 25111 Outboard Chord Length (m)	32.98
NASA SC(2)-0410 Wing Chord Length (m)	7.86

A8: Structural Parameters — Baseline BWB Configuration

Table 3: Structural parameters defining the baseline BWB configuration.

Parameter	**Value**
Spar Cap Area (m^2)	0.0052
CFRP Ultimate Strength (MPa)	900

A9: Parameter Correlation Matrix (Monte Carlo, Section 4.3)

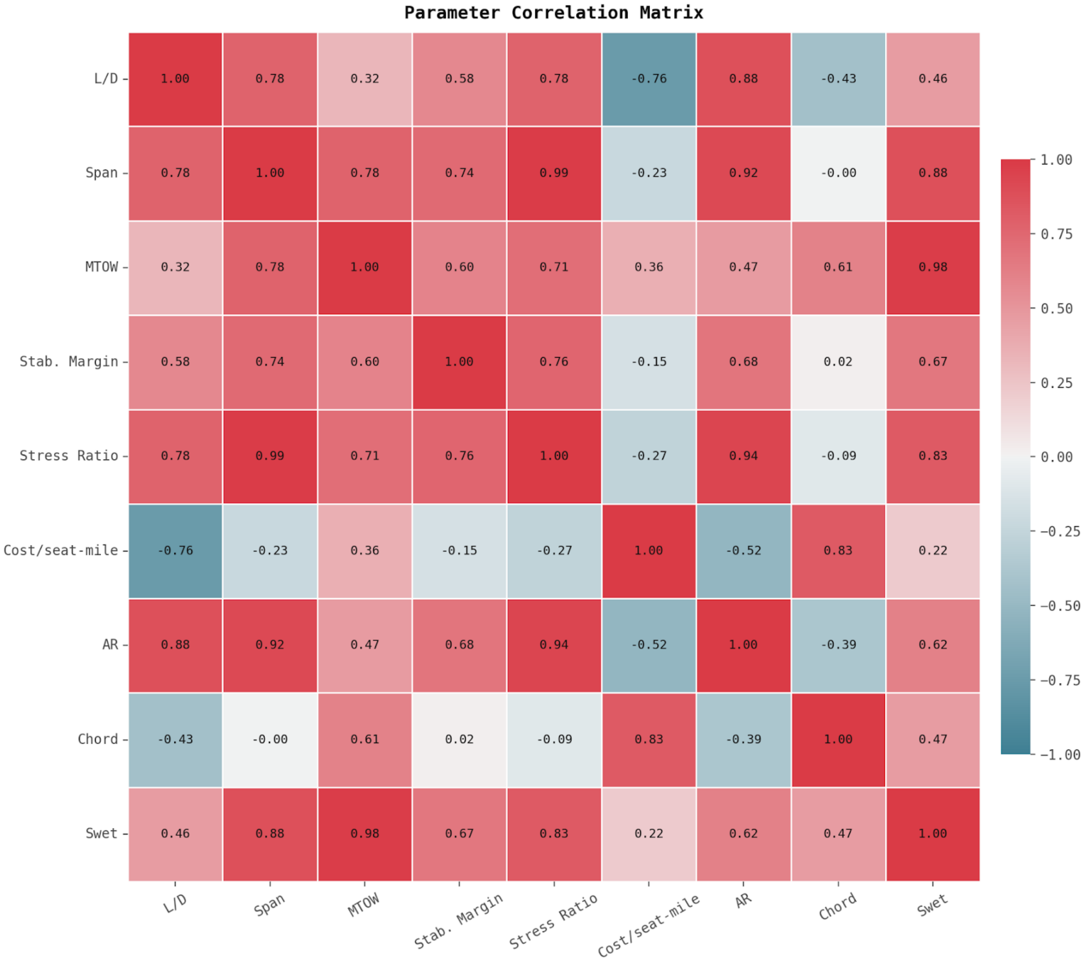

	L/D	Span	MTOW	Stab. Margin	Stress Ratio	Cost/seat-mile	AR	Chord	Swet
L/D	1.00	0.78	0.32	0.58	0.78	-0.76	0.88	-0.43	0.46
Span	0.78	1.00	0.78	0.74	0.99	-0.23	0.92	-0.00	0.88
MTOW	0.32	0.78	1.00	0.60	0.71	0.36	0.47	0.61	0.98
Stab. Margin	0.58	0.74	0.60	1.00	0.76	-0.15	0.68	0.02	0.67
Stress Ratio	0.78	0.99	0.71	0.76	1.00	-0.27	0.94	-0.09	0.83
Cost/seat-mile	-0.76	-0.23	0.36	-0.15	-0.27	1.00	-0.52	0.83	0.22
AR	0.88	0.92	0.47	0.68	0.94	-0.52	1.00	-0.39	0.62
Chord	-0.43	-0.00	0.61	0.02	-0.09	0.83	-0.39	1.00	0.47
Swet	0.46	0.88	0.98	0.67	0.83	0.22	0.62	0.47	1.00

Figure 15: Parameter correlation matrix from the Monte Carlo sensitivity analysis, displaying Spearman rank correlation coefficients between key design and performance variables. Red indicates strong positive correlation and blue indicates strong negative correlation.

A10: Pareto Plot of L/D vs. MTOW (Monte Carlo, Section 4.3)

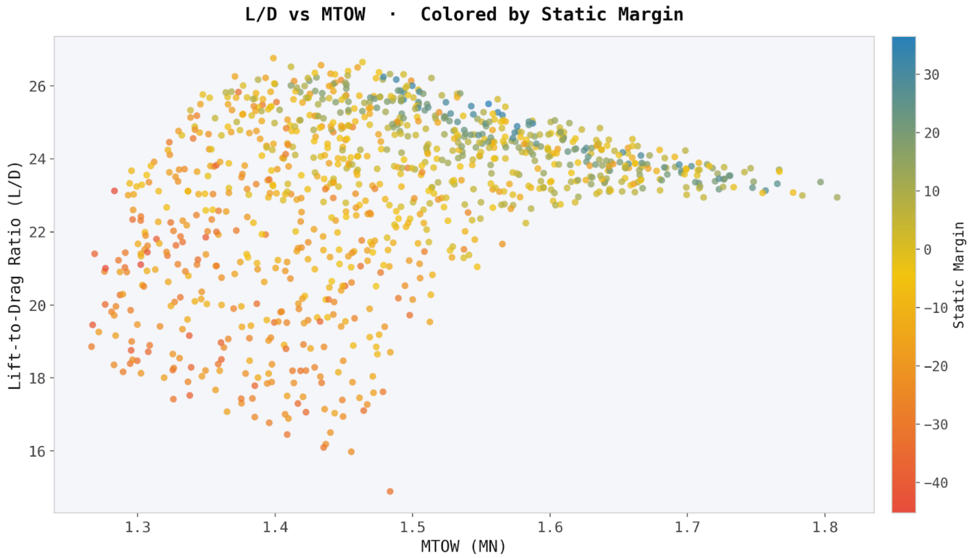

Figure 16: Scatter plot of cruise L/D versus MTOW from the Monte Carlo simulation, with each point colored by static margin. Higher L/D designs trend toward greater MTOW, with positive static margins concentrated among the top-performing configurations.

A11: Parallel Coordinates Plot (Monte Carlo, Section 4.3)

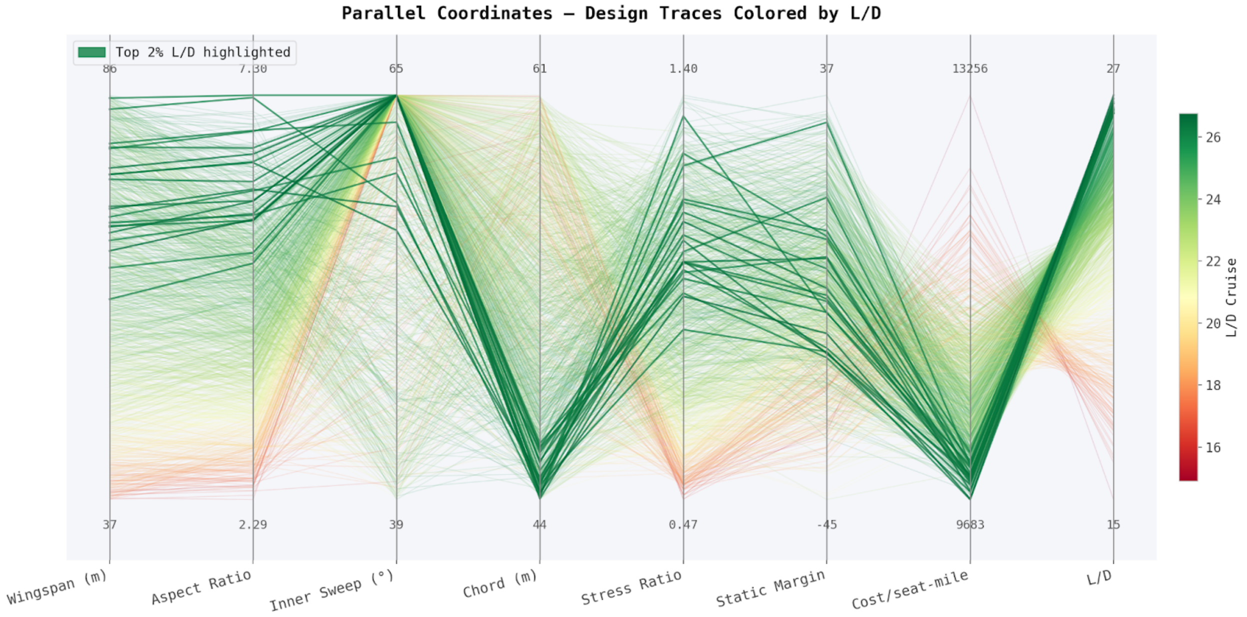

Figure 17: Parallel coordinates plot of key design parameters from the Monte Carlo simulation, with each trace colored by cruise L/D. The top 2% of L/D designs (highlighted in dark green) consistently converge toward high aspect ratio, moderate chord length, and low cost-per-seat-mile.